

We are IntechOpen, the world's leading publisher of Open Access books Built by scientists, for scientists

6,900

Open access books available

186,000

International authors and editors

200M

Downloads

Our authors are among the

154

Countries delivered to

TOP 1%

most cited scientists

12.2%

Contributors from top 500 universities



WEB OF SCIENCE™

Selection of our books indexed in the Book Citation Index
in Web of Science™ Core Collection (BKCI)

Interested in publishing with us?
Contact book.department@intechopen.com

Numbers displayed above are based on latest data collected.
For more information visit www.intechopen.com



Hybrid Silicon Nanowires for Solar Cell Applications

Adel Najar and Amine El Moutaouakil

Additional information is available at the end of the chapter

<http://dx.doi.org/10.5772/intechopen.74282>

Abstract

The global human population has been growing by around 1.1% per year; such growth rate will lead the humanity to cross the 10 billion-people threshold by the end of the first half of this century. Such increase is already putting a huge strain on the nonrenewable sources of energy like fossil fuel, which will run out and come to an end in few decades. Due to these social and economic trends, renewable sources of energy, such as solar cells, have attracted a huge interest as the ultimate alternative to solve humanity's problems. Among several emerging materials, porous silicon nanowires (PSiNWs) become an active research subject nowadays in photovoltaic application mainly due to its good light trapping effect. The etched nanowires obtained by using metal-assisted chemical etching method (MACE) can reach a low reflection in the visible range. Recently, hybrid silicon nanowires/organic solar cells have been studied for low-cost Si photovoltaic devices because the Schottky junction between the Si and organic material can be formed by solution processes at low temperature. In this chapter, we will present the synthesis of SiNWs and the last progress on the fabrication of hybrid solar cells using various organic semiconductors.

Keywords: silicon, nanowires, chemical etching, optical properties, solar cells

1. Introduction

Nanoscale silicon has been intensively investigated and explored for its applications in microelectronics, photonics, and biomedical sensors [1–3]. Specific efforts have been concentrated in the development of new silicon nanostructures, including quantum dots, nanowires, or porous silicon (PS). Porous silicon has attracted much attention, especially in enhancing photoemission. Much research efforts have been invested to realize an optical device with porous silicon [4–9], but the inefficiency [10] and instability [11] of optical characteristic in PS still remain. In addition, silicon nanowires (SiNWs) are also ideal candidate for the study of physics of low

dimensional systems. It has potential impact in realizing nanoscale interconnects and functional device elements in future nanoscale electronic and optoelectronic devices [12, 13]. The field of SiNWs synthesis represents an exciting and rapidly expanding research area. Considerable efforts have been devoted to the development of versatile and controllable methods for the synthesis of SiNW. These methods can be broadly classified as: (i) bottom-up and (ii) top-down approaches. The bottom-up approach involves the construction of desirable nanostructures from the basic components, i.e., from the atomic level to the nano- or microscale wires.

This method is useful for the fabrication of low-dimensional heterostructure-based devices in large quantities [14–18]. Using bottom-up, SiNWs were first obtained by vapor-liquid-solid (VLS) method [19], followed by an etching step to create nanowires. The VLS method has been implemented in a variety of techniques, such as pulsed laser deposition (PLD) [20, 21], gas-phase molecular beam epitaxy (GS-MBE) [22], chemical vapor deposition (CVD) [23, 24], laser ablation [25, 26], and oxide-assisted growth techniques [27].

Top-down approach seeks to fabricate SiNWs from high-quality single crystal silicon wafer or thin film. Silicon nanowires have also been realized using lithographically defined patterns, or spin-coating of nanospheres as etched mask [28] followed by etching of the nanowires using plasma processing technique. Metal-assisted chemical etching method (MACE) is a simple, cost-effective, and powerful semiconductor etching technique that can produce high aspect ratio semiconductor nanostructures. By combining with metal patterning lithography or nonlithographic patterning methods, accurate control of the nanowire orientation (vertical vs. slanted), size (nano vs. microscale), shape, architecture, density, length, and doping characteristics can be achieved readily at wafer scale.

The fabrication of silicon nanowires using the metal-assisted electroless etching method has also been adopted [29–33]. The silver (Ag) ions in an ionic solution of hydrofluoric acid (HF) and hydrogen peroxide (H_2O_2) have been used to prepare the arrays of SiNWs from single crystal wafers [34, 35]. The effects of various process parameters such as the etchant concentration of H_2O_2 , etching time, and postetch treatment on the morphology, and optical properties of the SiNWs have also been investigated [36]. The fabrication of nanowires using this method does not require complex sample preparation steps. Furthermore, this technique is effective, having high throughput and low cost. In this chapter, we will present the synthesis of PSiNWs and the last progress of hybrid solar cells based on these nanostructures.

2. Fabrication of porous silicon nanowires (PSiNWs)

Najar et al. detailed the fabrication of PSiNWs using Ag-assisted electroless etching method from an n-type Si wafer (100) with a resistivity of 0.01–0.02 ohm cm [33]. The Si wafers were cleaned using acetone followed by ethanol for 5 min in an ultrasonic bath. Next, the wafers were immersed in a piranha solution $\text{H}_2\text{SO}_4/\text{H}_2\text{O}_2$ (3:1) for 20 min to remove the organic deposits from the surface. The cleaned wafers were transferred into HF/AgNO₃ solution with a concentration of 4.8/0.005 M for Ag-deposition, followed by rinsing with de-ionized water. Then, the treated Si samples were etched in the HF/ H_2O_2 solution for 45 min. Finally, samples

were rinsed again for 10 min with HNO_3 solution to dissolve the excessive Ag nanoparticles (Ag NPs), leaving behind traces of Ag for catalyzing the etching reaction. Four samples were etched using HF concentration of 1.8, 2.8, 4.8, and 5.8 M, respectively, with a fixed H_2O_2 concentration of 0.5 M.

2.1. PSiNWs: Physical properties

Najar et al. studied the etching morphology of the synthesis of PSiNWs [32]. **Figure 1(a)** shows the scanning electron microscopy image of the vertically oriented PSiNWs having an average length of 13 μm after 75 min of wet etching. The nanowires distribute uniformly on the sample. **Figure 1(b)** shows the top view with tips of NWs congregates together, and the diameter of the congregated bundles is of several micrometers. These congregated bundles are uniformly distributed on the entire samples and confirmed from the cross-section images. The transmission electron microscopic (TEM) image of an individual nanowire is shown in **Figure 1(c)**, which shows that the nanowire has a diameter of ~ 150 nm.

A typical 2D bright-field TEM image used for volume reconstruction of the sample is presented in **Figure 2(a)–(c)**. The three successive longitudinal slices obtained from the reconstructed volume revealed a distribution of irregular size/shape vacuum spaces and silicon frame, constituting the PSiNWs.

A typical 3D-tomography observation was conducted using a TEM, and 3D reconstructions were achieved using a simultaneous iterative reconstruction algorithm of consecutive 2D slices in **Figure 2(d)** [32]. The pore sizes present a distribution from 10 to 50 nm, with an estimated measurement error of 10%, and these pores go inside the nanowire showing similar structure to porous silicon. An average distance between two neighboring pores of lower than 5 nm has been observed. These mesoporous structures are expected to show strong quantum confinement effects.

It is noted that mesopores are mostly found near the top of the nanowires with an average pore size between 10 and 40 nm. AgNPs were detected at the bottom section of the nanowires by

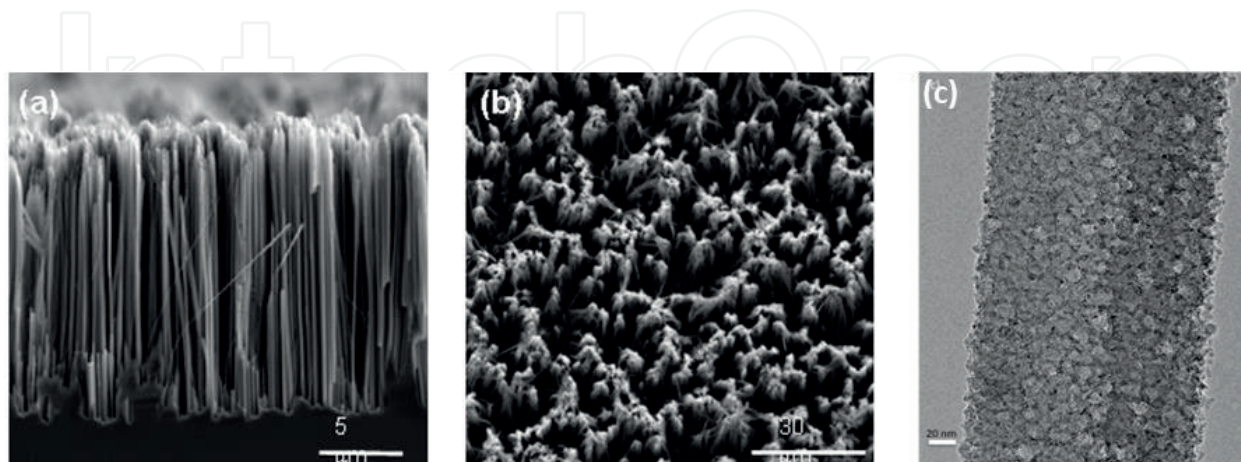


Figure 1. (a) Cross-sectional images of SEM micrograph of PSiNWs etched for 75 min, (b) top view micrograph of PSiNWs, (c) TEM image of individual nanowire, and inset of the FFT image [32].

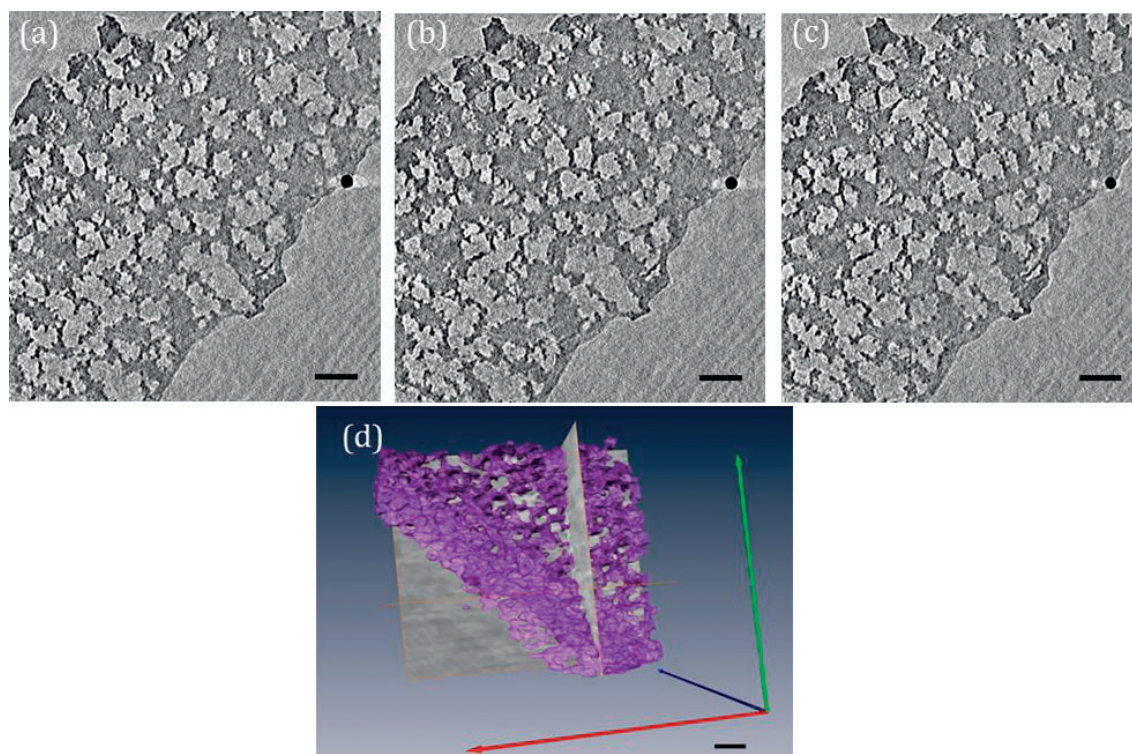


Figure 2. Panels (a), (b), and (c) represent three longitudinal slices extracted from the volume reconstruction of the PSiNW nanostructures revealing an area of highly porous medium. The bare scale is 50 nm. (d) 3D tomography TEM image of nanowires [32].

EDS analysis in STEM mode. Based on the SEM and TEM analyses, the following qualitative model for the formation of PSiNWs is proposed. In HF/H₂O₂ solution, part of the Ag is oxidized into Ag⁺ by H₂O₂ [37]. The Ag⁺ catalyzes the dissolution of Si through the formation of SiF₆²⁻.

It is apparent that the transport of Ag⁺ is isotropic while the AgNPs merely drop downward. Hence, the AgNPs facilitated the nanowire formation through vertical chemical etching, while the isotropic diffusion of Ag⁺ promoted lateral chemical etching and pore formation as illustrated in **Figure 3(a-i and a-ii)** [33].

The Ag⁺ may be chemically reduced by the n-type silicon nanowires [38] forming Ag particle that redeposited onto the sidewalls forming new Ag nucleation sites, and therefore the new localized lateral etching pathway. Furthermore, the nucleation of the AgNPs on the side walls would also reduce the Ag⁺ concentration locally and accelerates the Ag⁺ diffusion in the lateral direction. The laterally diffused Ag⁺ will continue to catalyze the chemical etching of the sidewalls of Si. Since the upper Si nanowires are exposed longer to the solutions, larger Si volume dissolves at the top (and creating more mesopores) than the bottom of the nanowires (**Figure 3(b-i and b-ii)** and **(c-i and c-ii)**), being consistent with the TEM image as shown in **Figure 2(a)**. Furthermore, increasing the HF concentration accelerates the process described in our qualitative model, with the Ag → Ag⁺ + e⁻ reversible reaction that continues to penetrate the nanowires laterally to catalyze the HF/H₂O₂ chemical reaction forming mesopores. Eventually, the mesopores merged leading to a reduction in length and pore density, with the formation of conical PSiNWs as illustrated in **Figure 3(d-i and d-ii)**.

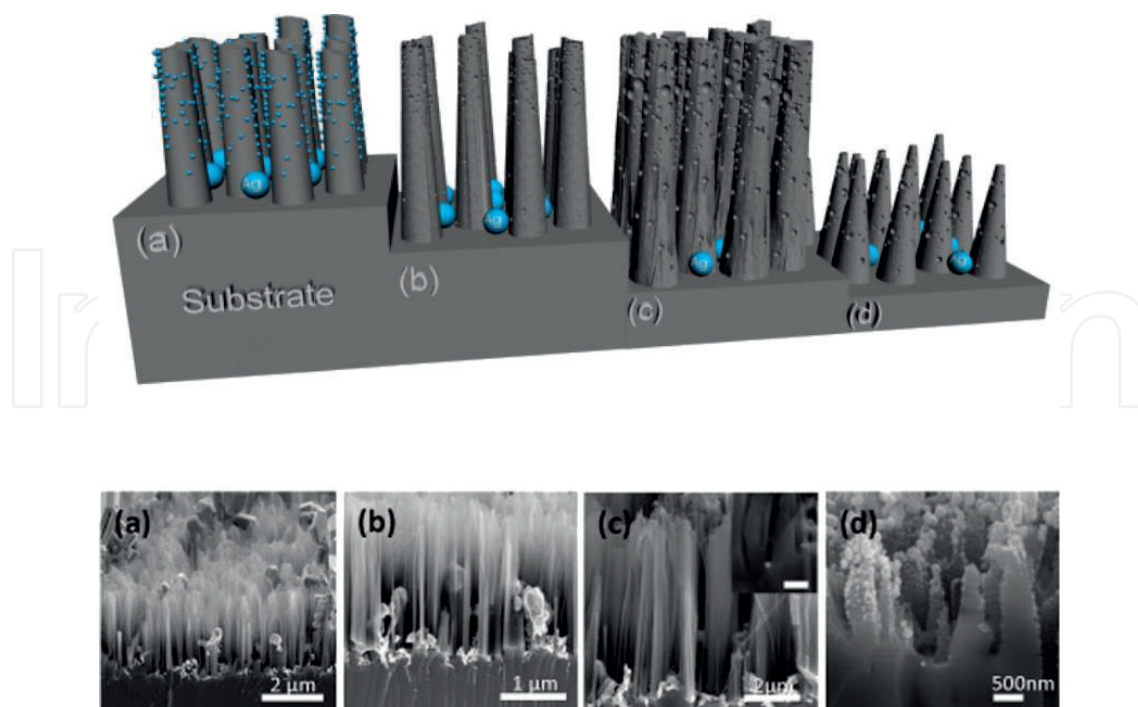


Figure 3. (a-i)–(d-i) The schematic illustration of the proposed qualitative etching model for the formation of PSiNWs using Ag-assisted HF/H₂O₂ electroless etching technique. (a-ii)–(d-ii) The corresponding SEM micrographs, prepared using various HF concentrations [33].

In this way, the higher H₂O₂ concentration increases the amount of out-diffused Ag⁺, and the increase of doping concentration increases the amount of weak defective points in the silicon lattice; both are important factors for the initiation of additional etching pathways in addition to the vertical etch, which explains the observation of the increased porosity with increasing H₂O₂ concentration during the etching of highly doped n-Si wafers.

The heavy doping silicon wafer-induced porosification can be understood by a thermodynamic model that describes charge transport across the silicon-electrolyte interface driven by potential energy (**Figure 4(a)**). To et al. present a model to explain the etching mechanism [39]. In **Figure 4(a)**, the electron transports from Si to Ag⁺ ions, which is composed of the processes I-IV at the Si/electrolyte interface. Electrons at E_F of Si wafers migrate to the interface by overcoming a potential energy barrier ΔΦ, consisting of the excitation barrier (E_{CB}–E_F, the process I) and the band edge bending in space charge layer (SCL) (E_{CB'S}–E_{CB'}, the process II). Owing to the mismatch of E_{CB,S} with E_{Ag⁺}, electrons are apt to relaxing to surface states (E_{SS}) aligned with E_{Ag⁺} (the process III) followed by the resonant migration to E_{Ag⁺} (the process IV). The increase in the doping level not only up shifts E_F toward E_{CB} to reduce ΔΦ, but also makes the SCL thinner to promote electron tunneling through the SCL (**Figure 4(b)**), to facilitate the process I and II. Hence, a large amount of Ag⁺ ions nucleate on the surface and [Ag⁺] (i.e., concentration of Ag⁺ ions) is significantly reduced in the electrolyte. Low [Ag⁺] can support only a portion of Ag nuclei to grow and scratch the bulk Si. The rest of the nongrown Ag nuclei will undergo a random scratching in a short period of time to porosify SiNWs and the bulky wafer (**Figure 4(c)**). Since the scratching of growing Ag NPs is limited by the diffusion of Ag⁺ ions with low [Ag⁺], the random porosification tends to be faster than the NP scratching. Consequently, the

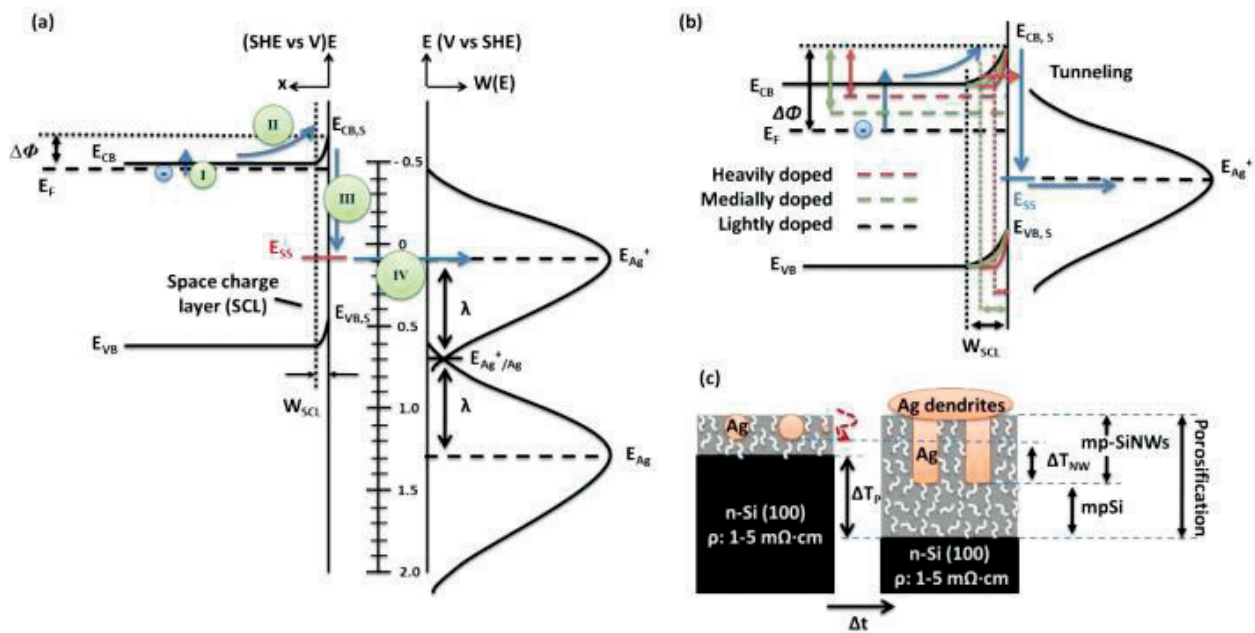


Figure 4. (a) Quasi-quantitative energy diagram at the silicon-electrolyte interface, at the beginning of one-MACE of n++ type Si(100). The energy is referred to standard hydrogen electrode (SHE) potential. Heavily doped n-Si has Fermi energy (E_F), valence, and conduction band in the bulk (E_{VB} and E_{CB}) and at the interface ($E_{VB,S}$ and $E_{CB,S}$), and space charge layer (SCL) with a width W_{SCL} . $\Delta\Phi$ is an energy barrier between E_F and $E_{CB,S}$. $E_{Ag^+/Ag}$, E_{Ag^+} , and E_{Ag} represent the potential energy of the redox pair, Ag^+ and Ag in the electrolyte, respectively. λ is the reorientation energy. The light blue sphere represents an electron at E_F , and the I-IV processes denote a subsequent series of electron migration from the bulk to interface. (b) Energy diagram with variation of doping levels in n-Si(100). (c) Schematic of the one-MACE evolution. For clarity, only one nongrown Ag nucleus scratching the wafer in the mpSi is shown, marked by a red dashed line. Within a period of time Δt , the evolution of the porosification and mesoporous SiNWs are denoted by ΔT_p and ΔT_{NW} respectively [39].

electrochemical porosification tends to generate a hybrid structure composed of an array of mpSiNWs on mpSi (**Figure 4 (a)–(d)**). On the contrary, the light and media doping increases $\Delta\Phi$ to prevent Ag^+ ions from severely consuming. High $[Ag^+]$ substantially supports most Ag NPs grow and scratch the wafer to create SiNWs, and effectively suppresses the porosification. This model can also account for the creation of mesoporous SiNWs via one-MACE of p++ type Si.

2.2. HF concentrations vs. morphology of PSiNWs

The modification of HF or H_2O_2 concentrations affects the morphology of PSiNWs. In the presence of Ag catalyst, an increase in HF or H_2O_2 concentration in electroless etching method is analogous to an increase in the current density in electrochemical-based methods [40, 41]. In both cases, increasing the H_2O_2 or HF concentration increases the oxidation rate and dissolution rate, respectively, resulting in nanostructures with varying optical properties. In **Figure 5(a)–(h)**, Najjar et al. shows the cross-sectional SEM micrographs and TEM images acquired from the NW samples grown with HF concentrations of 1.8, 2.8, 4.8, and 5.8 M in a fixed H_2O_2 concentration of 0.5 M [33].

The variation of NWs length and NWs diameter with increasing HF concentrations was measured and analyzed using SEM and TEM, and the results are tabulated in **Table 1**. The NWs length shows significant changes, while the NWs diameter varies from 80 to 210 nm for samples

indicating the dominant effect of vertical etching enhanced by Ag catalyst with preferential etching along the low atomic density plane in [001]. An increase in aspect ratio from about 9 to 12 and 27 has been calculated for NWs samples etched with 1.8, 2.8, and 4.8 M HF concentration

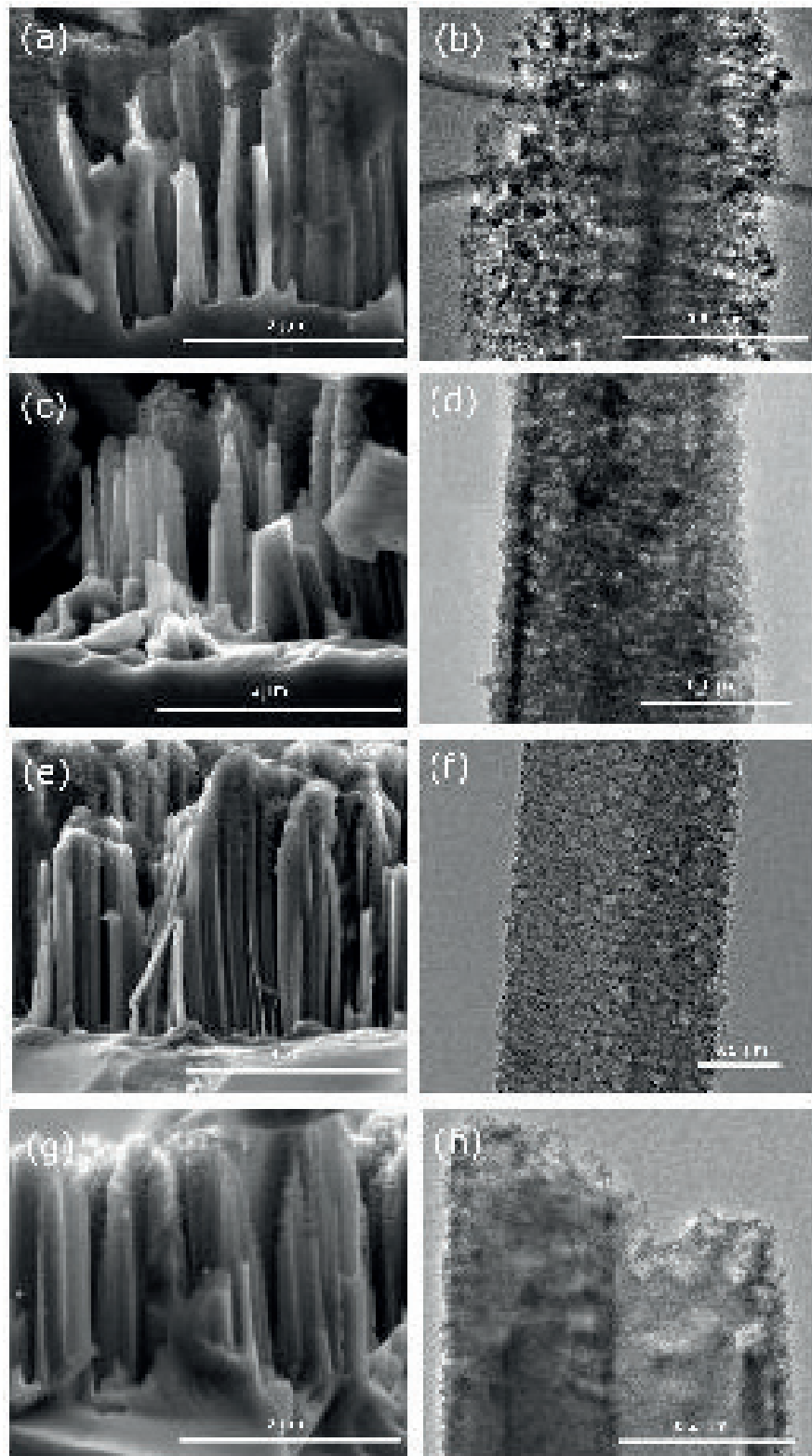


Figure 5. (a)–(h) SEM and TEM micrographs of PSiNWs fabricated with increasing HF concentration from 1.8, 2.8, 4.8, up to 5.8 M [33].

PSiNWs physical parameters	HF concentration			
	1.8 M	2.8 M	4.8 M	5.8 M
NWs length (μm)	1.3–1.8	2–2.2	4.8–5.3	1.6–1.8
NWs diameter (nm)	160–210	100–180	80–200	150–200
Aspect ratio (longest length/largest diameter)	~9	~12	~27	~9

Table 1. Effect of HF concentration on PSiNWs length, NWs diameter, and aspect ratio analyzed from SEM micrographs [33].

(**Figure 5(a)**, (**c**), and (**e**)). However, the aspect ratio reduces to about 9 for NWs etched with (**Figure 5(g)**) signifying a change in etching mechanism with faster lateral chemical etch.

2.3. Effect of HF concentration on PL

It is known that the mesoporous silicon nanostructure gives rise to strong visible emission [42]. Optical properties of the PSiNWs samples have been investigated using PL spectroscopy. **Figure 6(a)** shows the PL spectra of the samples etched with HF concentrations of 1.8, 2.8, 4.8, and 5.8 M with a constant H_2O_2 concentration of 0.5 M. It is observed that the asymmetric PL spectra have two dominant peaks around 700 and 760 nm. The sample etched with 4.8 M HF concentration has an additional hump at 670 nm. The highest PL peak at 760 nm is related to the emission from Si–O bond [42, 43].

In our case, we observe in **Figure 6(a)** that the increase in integrated intensities of the broad-band PL emissions correlates well with the increase in pore densities for samples etched using 1.8–4.8 M HF concentrations. With an HF concentration of 5.8 M, a reduction in PL integrated intensity is again consistent with a reduction in the pore density of PSiNWs.

After HNO_3 and HF treatments for 5 min to remove the oxide, all samples show similar PL peak wavelength at 800 nm (**Figure 6(c)**). However, samples without HF treatment show a significant blueshift with PL wavelength peak at 700 nm (**Figure 6(a)**). This blueshift and increase of PL intensity have been attributed to the presence of defect states in Si–Ox.

This has been correlated with the redshift of PL spectrum that suggests the interfacial between Si and surface oxide, as well as the quantum confinement effect, and plays a critical role in the light emission process (i.e., the presence of nanocrystallites with size <5 nm that has been confirmed by HRTEM).

Several mechanisms have been proposed to explain the origin of strong PL emission for the indirect bandgap silicon material. These include (i) the quantum confinement effects of free excitons within the Si-nanocrystallites and (ii) SiO_x/Si interface defects and/or defect states in the surface oxide, related to Si–O bond [42, 44, 45]. Comparing the PL spectra before and after the HF treatment, we believe that existence of oxide plays a significant role in changing the emission property of the nanowires.

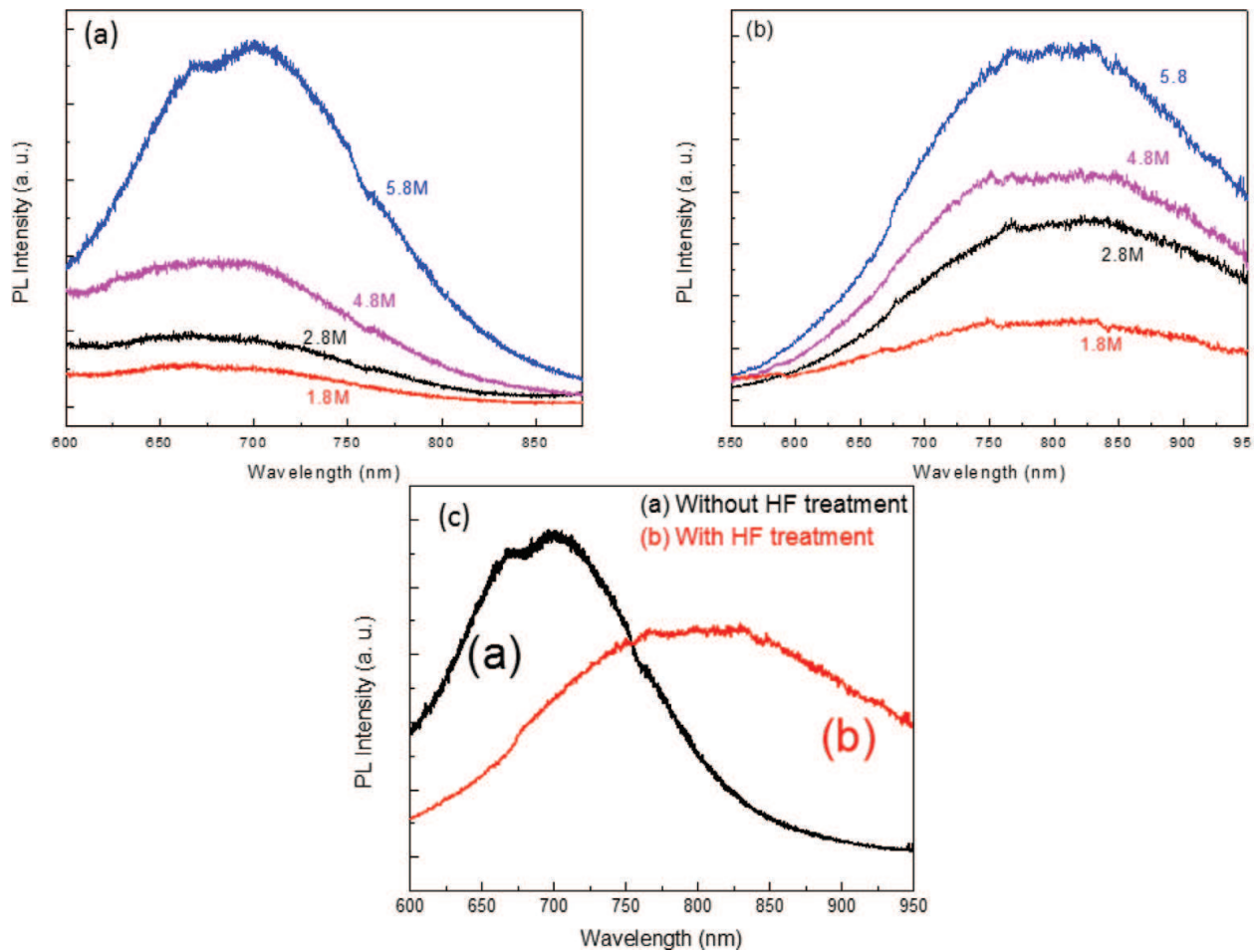


Figure 6. PL spectra of PSiNWs as a function of HF concentration etched for 45 min (a): 1.8, 2.8, 4.8, and 5.8 M, (b) after HNO₃ treatment followed by HF (5%), and (c) with and without HF treatment [33].

The quantum confinement effect dictates that the characteristic size of the Si-nanocrystallites should be less than the Bohr radius of the free exciton of bulk Si, which is around 5 nm [46]. From the TEM analysis, Si-nanocrystallites of <5 nm has been observed (**Figure 7(a)**). The inset of **Figure 7(a)** shows the calculated fast-Fourier transform (FFT) of PSiNWs prepared using 4.8 M HF concentration. The FFT revealed the spatial frequencies corresponding to {111}, {220}, and {311} d-spacing of Si crystal structure. The presence of these d-spacing implies that the PSiNW was oriented along the <110> direction. This was expected as the (001) Si wafer was used to fabricate the NWs, and etching was vertical with respect to the substrate surface. Also, the energy-filtered TEM analysis of the top region of the PSiNW, as shown in **Figure 7(b)**, confirms the existence of Si nanocrystallites and silica amorphous structures, indicating the possible strong PL emission from the highly quantum-confined Si nanocrytallite structures. This prediction correlates positively with our previous discussion on the effect of pore density on PL enhancement. The above argument further confirms our observation that samples etched with HF concentration of 5.8 M (i.e., with low pore and Si-nanocrystallites densities) results in a decrease in PL intensity. The evolution of PL peak intensity with HF concentration is hence consistent with the physical changes in the PSiNWs developed in our etching model.

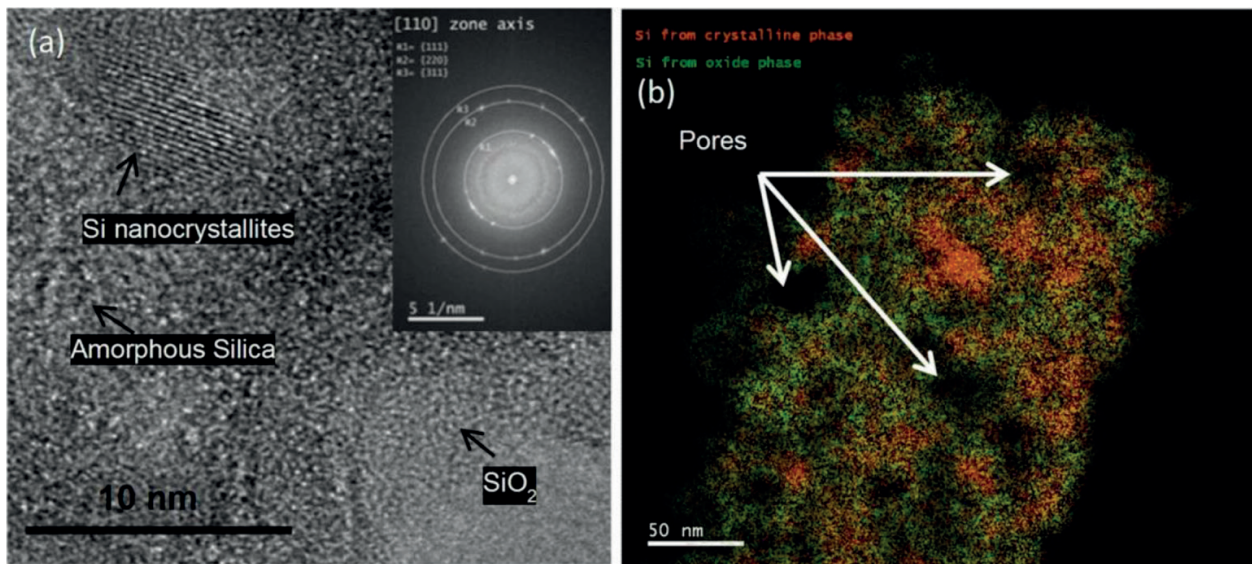


Figure 7. (a) HRTEM and (b) EFTEM analyses of the top section of a PSiNW etched using 4.8 M concentration of HF [33].

However, SiO_2 alone should not give rise to the PL emission; rather, defect states would contribute to PL emission. Indeed, Najar et al. observed Si^{1+} (Si_2O) and Si^{3+} (Si_2O_3) using X-ray photoelectron spectroscopy (XPS) signatures, which may originate from dangling bonds and volumetric stress that distorted the PSiNWs forming localized defect states.

Therefore, the emissions from surface/defect states in oxide may contribute to the red PL emission, in agreement with the results obtained in [47], in addition to the contribution from quantum confinement effect.

3. Organic-inorganic hybrid nanowire solar cells

As a platform for cost-effective crystalline Si (c-Si) solar cells, an organic-inorganic hybrid structure has been proposed to replace the conventional p-n junction. The hybrid structure is composed of a transparent conducting polymer and c-Si [48, 49]. A Schottky junction at the conducting polymer/c-Si interface can easily be created using a simple spin coating process at room temperature, while a conventional Si p-n junction is formed via a high-temperature doping process [50]. In order to enhance the light-trapping efficiency, Si nanostructures such as nanopillars [49] and nanowires [51] have been applied, leading to an increase in the short-circuit current density (J_{sc}).

Han-Dom Um et al. demonstrate an embedded metal electrode for highly efficient organic-inorganic hybrid nanowire solar cells as shown in **Figure 8** [52]. The electrode proposed here is an effective alternative to the conventional bus and finger electrode, which leads to a localized short circuit at a direct Si/metal contact and has a poor collection efficiency due to a nonoptimized electrode design. In this design, an Ag/ SiO_2 electrode is embedded into a Si substrate while being positioned between Si nanowire arrays underneath poly(3,4-ethylenedioxythiophene):poly(styrenesulfonate) (PEDOT:PSS), facilitating suppressed recombination at

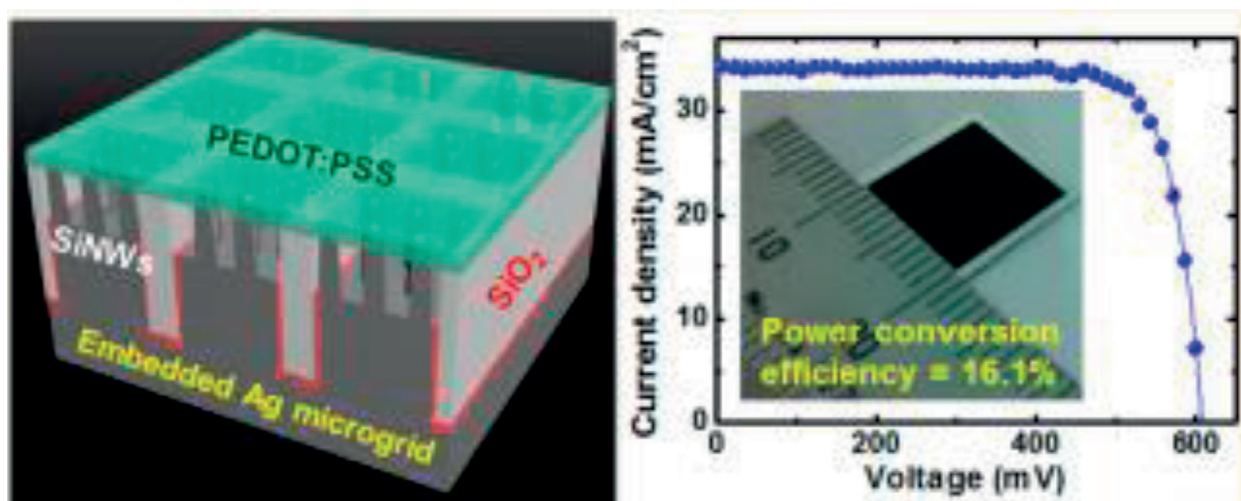


Figure 8. Embedded metal electrode for highly efficient organic-inorganic hybrid nanowire solar cells, and I-V characteristic of the solar cell [52].

the Si/Ag interface and notable improvements in the fabrication reproducibility. With an optimized microgrid electrode, the 1-cm² hybrid solar cells exhibit a power conversion efficiency of up to 16.1% with an open-circuit voltage of 607 mV and a short-circuit current density of 34.0 mA/cm². This power conversion efficiency is more than twice as high as that of solar cells using a conventional electrode. The microgrid electrode significantly minimizes the optical and electrical losses. This reproducibly yields a superior quantum efficiency of 99% at the main solar spectrum wavelength of 600 nm. In particular, the solar cells exhibit a significant increase in the fill factor of 78.3% compared to that of a conventional electrode (61.4%), this is because of the drastic reduction in the metal/contact resistance of the 1 μ m-thick Ag electrode. Hence, the use of this embedded microgrid electrode in the construction of an ideal carrier collection path presents an opportunity in the development of highly efficient organic-inorganic hybrid solar cells.

Liu et al. fabricated a hybrid silicon nanowire/polymer heterojunction solar cell combined with a polypyrrole-based supercapacitor as shown in **Figure 9**, to harvest solar energy and store it [53]. By efficiency enhancement of the hybrid nanowire solar cells and a dual-functional titanium film serving as a conjunct electrode of the solar cell and supercapacitor, the integrated system is able to yield a total photoelectric conversion to storage efficiency of 10.5%, which is the record value in all the integrated solar energy conversion and storage system. This system may not only serve as a buffer that diminishes the solar power fluctuations from light intensity, but also pave its way toward cost-effective high-efficiency self-charging power unit. Finally, an integrated device based on ultrathin Si substrate is demonstrated to expand its feasibility and potential application in flexible energy conversion and storage devices.

Organic-inorganic hybrid solar cells based on n-type crystalline silicon and poly(3,4-ethylenedioxythiophene)-poly(styrenesulfonate) exhibited promising efficiency along with a low-cost fabrication process (**Figure 10**). Zhang et al. fabricated ultrathin flexible silicon substrates, with a thickness as low as tens of micrometers, which were employed to fabricate hybrid solar cells to reduce the use of silicon material [54]. To improve the light-trapping ability,

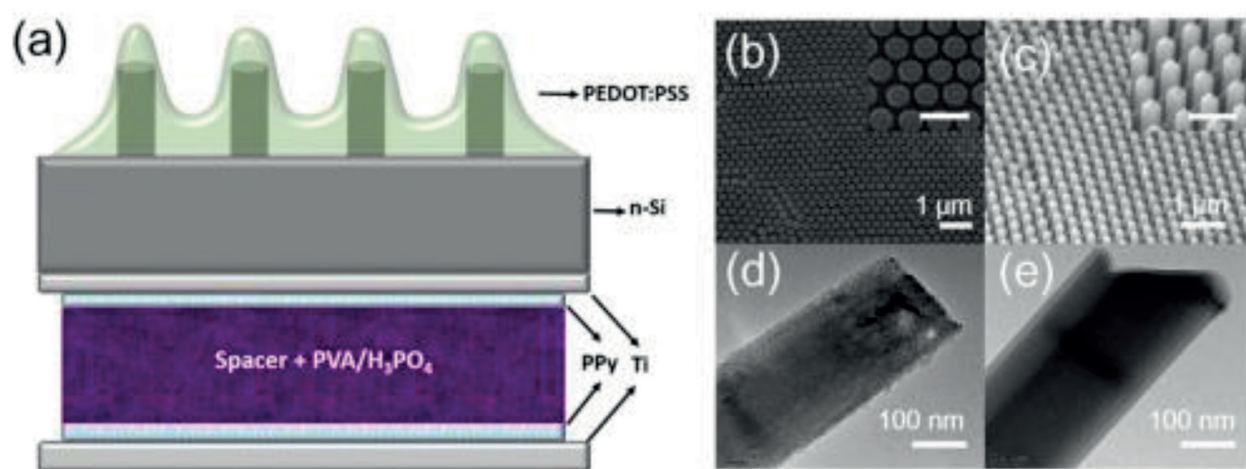


Figure 9. (a) Schematic of the integrated hybrid device containing a SiNW-based heterojunction solar cell and a polypyrrole-based supercapacitor. (b) SEM image of as-fabricated SiNW. (c) SEM image of SiNW after 2 h of PCl₅ treatment. (d) TEM image of a single as-fabricated Si nanowire. (e) TEM image of a single Si nanowire after 10 min of methylation treatment. The scale bars are 500 nm in the insets of (b) and (c) [53].

nanostructures were built on the thin silicon substrates by a metal-assisted chemical etching method (MACE). However, nanostructured silicon resulted in a large amount of surface-defect states, causing detrimental charge recombination. Here, the surface was smoothed by solution-processed chemical treatment to reduce the surface/volume ratio of nanostructured silicon. Surface-charge recombination was dramatically suppressed after surface modification with a chemical, associated with improved minority charge carrier lifetime. As a result, a power conversion efficiency of 9.1% was achieved in the flexible hybrid silicon solar cells, with a substrate thickness as low as $\sim 14 \mu\text{m}$, indicating that interface engineering was essential to improve the hybrid junction quality and photovoltaic characteristics of the hybrid devices.

As shown in **Figure 10(b)**, the leakage current of the TMAH-treated nanostructured silicon devices is much lower than that of the untreated silicon devices, suggesting that the junction quality is improved. Furthermore, the J_{SC} of the hybrid devices based on different surface morphologies is consistent with the external quantum efficiency (EQE) spectra, as shown in **Figure 10(c)**. The device based on $\sim 14\text{-}\mu\text{m}$ thick planar silicon without TMAH treatment gives a J_{SC} of 18.4 mA cm^{-2} , a V_{OC} of 0.56 V, and an FF of 0.75, achieving a PCE of 7.9%. The previously reported ultrathin planar silicon device with a thickness of $8.6 \mu\text{m}$ yields a PCE of 5.2% [55]. Here, the reduced J_{SC} for the device based on $\sim 14\text{-}\mu\text{m}$ thick planar silicon is ascribed to the high light reflection of the planar silicon surfaces, which resulted in poor light absorption compared to that of a thicker device. In comparison with planar devices, nanostructured silicon solar cells exhibit a larger J_{SC} value, indicating that the incident light could be effectively absorbed by nanostructured silicon. The absorption spectra of the planar and nanostructured silicon with or without TMAH treatment are shown in **Figure 10(e)**. According to the absorption spectra, the nanostructured silicon exhibits an obviously better light absorption over a broad spectrum from the visible to the near-infrared range compared to that of planar silicon.

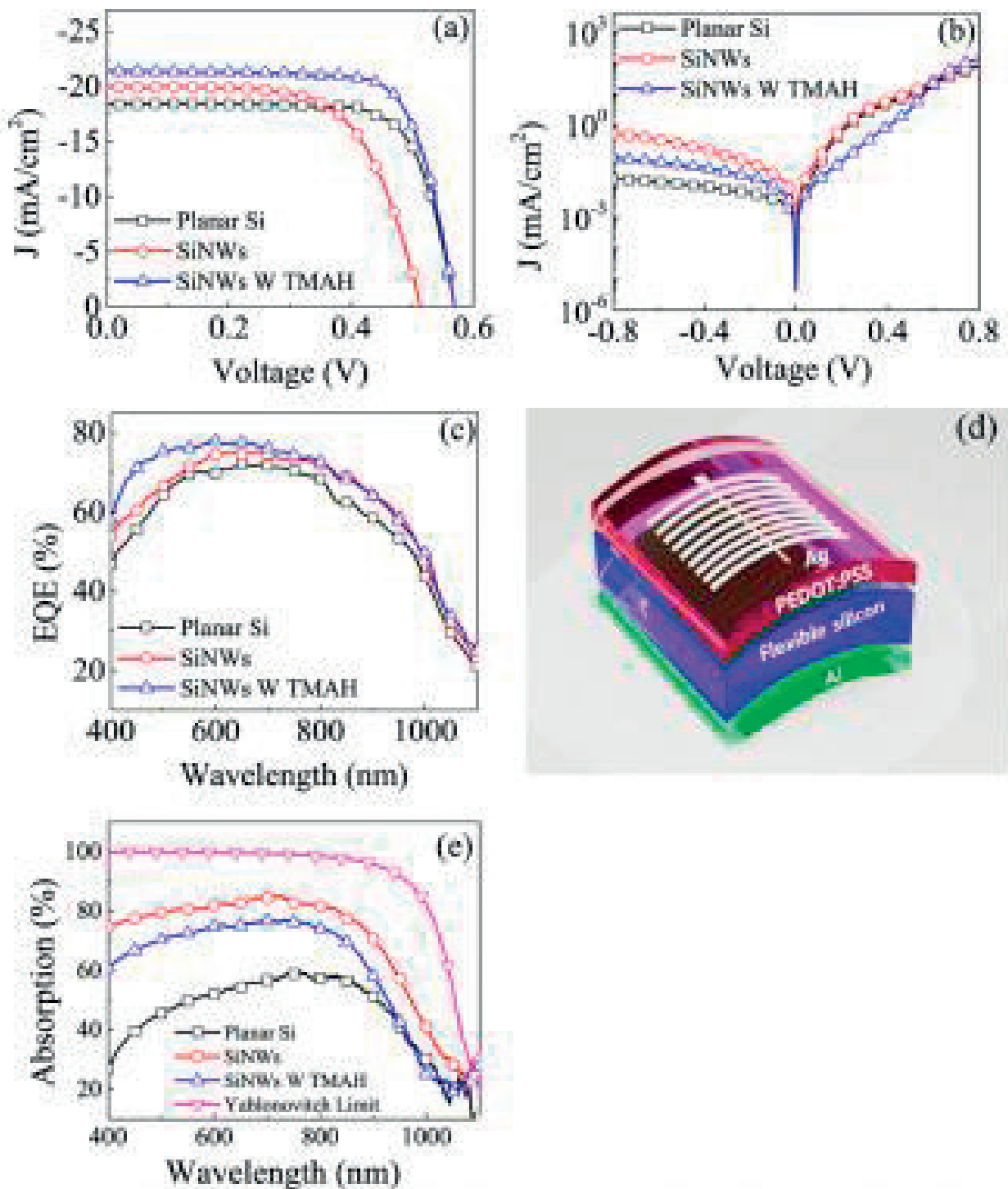


Figure 10. Electric-output characteristics of the PEDOT:PSS/Si devices under different surface conditions. (a) J–V curves under illumination at 100 mW cm⁻², (b) J–V curves in the dark, and (c) EQE spectra of devices based on silicon substrates with a planar surface (black), an as-prepared nanostructured silicon surface (red), and a TMAH-treated nanostructured silicon surface (blue). (d) Schematic device structure of the flexible PEDOT:PSS/Si hybrid solar cell. (e) Absorption spectra of silicon substrates with a planar surface, an as-prepared nanostructured silicon surface, a TMAH-treated nanostructured silicon surface, and upon Yablonovitch limit simulation [54].

4. Conclusion

In summary, facile silicon surface modification methods based on one or two MACE to synthesis PSiNWs were presented. The change in morphology based on HF or H₂O₂ effect was presented. Furthermore, this change also affects the optical properties specially the photoluminescence and compensates the poor light absorption of the planar silicon substrate. Several emerging strategies result in high-performance hybrid solar cells based on PSiNWs were presented. These strategies are based on the organic materials or/and the design of the solar cells or on the grid electrode as a contact. These findings could be potentially employed to further reduce the fabrication cost of silicon solar cells by reducing the consumption of silicon materials and increasing their efficiency.

Author details

Adel Najar^{1*} and Amine El Moutaouakil²

*Address all correspondence to: adel.najar@uaeu.ac.ae

1 Department of Physics, College of Sciences, UAE University, UAE

2 Electrical Engineering Department, College of Engineering, UAE University, UAE

References

- [1] Zhao XY, Wei CM, Yang L, Chou MY. Quantum confinement and electronic properties of silicon nanowires. *Physical Review Letters*. 2004;**92**:236805
- [2] Cui Y, Lieber CM. Functional nanoscale electronic devices assembled using silicon nanowire building blocks. *Science*. 2001;**291**:851
- [3] Lieber CM, Wang ZL, Nanowires F. *MRS Bulletin*. 2007;**32**:99
- [4] Najar A, Charrier J, Ajlani H, Lorrain N, Haesaert S, Oueslati M, Haji L. Optical gain at 1.53 μm in Er³⁺-Yb³⁺ co-doped porous silicon waveguides. *Materials Science and Engineering B*. 2008;**146**:260
- [5] Najar A, Lorrain N, Ajlani H, Charrier J, Oueslati M, Haji H. Er³⁺ doping conditions of planar porous silicon waveguides. *Applied Surface Science*. 2009;**256**:581
- [6] Najar A, Ajlani H, Charrier J, Lorrain N, Haesaert S, Oueslati M, Haji L. Optical study of erbium-doped-porous silicon based planar waveguides. *Physica B: Condensed Matter*. 2007;**396**:145
- [7] Najar A, Charrier J, Lorrain N, Haji L, Oueslati M. Optical gain measurements in porous silicon planar waveguides codoped by erbium and ytterbium ions at 1.53 μm . *Applied Physics Letters*. 2007;**91**(12):121120-121120

- [8] Najar A, Charrier J, Ajlani H, Lorrain N, Elhouichet H, Oueslati M, Haji L. Optical properties of erbium-doped porous silicon waveguides. *Journal of Luminescence*. 2006; **121**(2):245-248
- [9] Najar A, Elhouichet H, Lorrain N. Oueslati Excitation mechanisms and localization sites of erbium-doped porous silicon M. *Applied Surface Science*. 2006;**252**(16):5808-5813
- [10] Koyama H, Nakagawa T, Ozaki T, Koshida N. Post-anodization filtered illumination of porous silicon in HF solutions: An effective method to improve luminescence properties. *Applied Physics Letters*. 1994;**65**:1656
- [11] Canham LT, Houlton MR, Leong WY, Pickering C, Keen JM. Atmospheric impregnation of porous silicon at room temperature. *Journal of Applied Physics*. 1991;**70**:422-431
- [12] Huang Y, Duan X, Lieber CM. Nanowires for integrated multicolor nanophotonics. *Small*. 2005;**1**:142
- [13] Bohr MT. Nanotechnology goals and challenges for electronic applications. *IEEE Transactions on Nanotechnology*. 2002;**1**:56
- [14] Najar A, Jouiad M. Synthesis of InGaN nanowires via metal-assisted photochemical electroless etching for solar cell application. *Solar Energy Materials and Solar Cells*. 2017. DOI: 10.1016/j.solmat.2017.06.008
- [15] Xia YN, Yang PD, Sun YG, Wu Y, Mayers N, Gates B, Yin Y, Kim F, Yan H. One-dimensional nanostructures: Synthesis, characterization, and applications. *Advanced Materials*. 2003;**15**:353
- [16] Najar A, Gerland M, Jouiad M. Porosity-induced relaxation of strains in GaN layers studied by means of micro-indentation and optical spectroscopy. *Journal of Applied Physics*. 2012;**111**(9):093513-093513
- [17] Slimane AB, Najar A, Elafandy R, San-Román-Alerigi D, Anjum D, Ng TK, Ooi BS. On the phenomenon of large photoluminescence. Red shift in GaN nanoparticles. *Nanoscale Research Letters*. 2013;**8**:342-348
- [18] Najar A, Shafa M, Anjum D. Synthesis, optical properties and residual strain effect of GaN nanowires generated via metal-assisted photochemical electroless etching. *RSC Advances*. 2017;**7**(35):21697-21702
- [19] Wagner RS, Ellis WC. Vapor-liquid-solid mechanism of single crystal growth. *Applied Physics Letters*. 1964;**4**:89-90
- [20] Morales AM, Lieber CM. A laser ablation method for the synthesis of crystalline semiconductor nanowires. *Science*. 1998;**279**:208
- [21] Zhang YF, Tang YH, Wang N, Yu DP, Lee CS, Bello I, Lee ST. Silicon nanowires prepared by laser ablation at high temperature. *Applied Physics Letters*. 1998;**72**:1835-1837
- [22] Schubert L, Werner P, Zakharov ND, Gerth G, Kolb FM, Long L, Geosele U, Tan TY. Silicon nanowhiskers grown on 111 Si substrates by molecular-beam epitaxy. *Applied Physics Letters*. 2004;**84**:4968-4970

- [23] Stelzner T, Pietsch M, Andrea G, Falk F, Ose E, Christiansen S. Silicon nanowire-based solar cells. *Nanotechnology*. 2008;**19**:295203
- [24] Lu M, Li MK, Kong LB, Guo XY, Li HL. Silicon quantum-wires arrays synthesized by chemical vapor deposition and its micro-structural properties. *Chemical Physics Letters*. 2003;**374**:542-547
- [25] Au FCK, Wong KW, Tang YH, Zhang YF, Bello I, Lee ST. Electron field emission from silicon nanowires. *Applied Physics Letters*. 1999;**75**:1700
- [26] Yu DP, Lee CS, Bello I, Sun XS, Tang YH, Zhou GW, Bai ZG, Zhang Z, Feng SQ. Synthesis of nano-scale silicon wires by excimer laser ablation at high temperature. *Solid State Communications*. 1997;**105**:403
- [27] Wang N, Tang YH, Zhang YF, Lee CS, Bello I, Lee ST. Si nanowires grown from silicon oxide. *Chemical Physics Letters*. 1999;**299**:237-242
- [28] Juhasz R, Kylmeanen K, Galeckas A, Linnros J. Size-reduced silicon nanowires: Fabrication and electrical characterization. *Materials Science and Engineering*. 2005;**25**:733-737
- [29] Hochbaum AI, Gargas D, Hwang YJ, Yang P. Single crystalline mesoporous silicon nanowires. *Nano Letters*. 2009;**9**:3550-3554
- [30] Kumar D, Srivastava SK, Singh PK, Sood KN, Singh VN, Dilawar N, Husain M. Room temperature growth of wafer-scale silicon nanowire arrays and their Raman characteristics. *Journal of Nanoparticle Research*. 2010;**12**:2267-2276
- [31] Srivastava SK, Kumar D, Singh PK, Kar M, Kumar V, Husain M. Excellent antireflection properties of vertical silicon nanowire arrays. *Solar Energy Materials & Solar Cells*. 2010;**94**:1506-1511
- [32] Najar A, Charrier J, Pirasteh P, Sougrat R. Ultra-low reflection porous silicon nanowires for solar cell applications. *Optics Express*. 2012;**20**:16861-16870
- [33] Najar A, Slimane A B, Hedhili MN, Anjum D, Sougrat R, Ng TK, Ooi BS. Effect of hydrofluoric acid concentration on the evolution of photoluminescence characteristics in porous silicon nanowires prepared by Ag-assisted electroless etching. *Journal of Applied Physics*. 2012;**112**:033502-033502
- [34] Peng KQ, Yan YJ, Gao SP, Zhu J. Synthesis of large-area silicon nanowire arrays via self-assembling nanoelectrochemistry. *Advanced Materials*. 2002;**14**:1164
- [35] Qiu T, Wu XL, Mei YF, Wan GJ, Chu PK, Siu GG. From Si nanotubes to nanowires: synthesis, characterization, and self-assembly. *Journal of Crystal Growth*. 2005;**277**:143-148
- [36] Qu Y, Zhou H, Duan X. Porous silicon nanowires. *Nanoscale*. 2011;**3**:4060
- [37] Zhang ML, Peng KP, Fan X, Jie JS, Zhang RQ, Lee ST, Wong NB. Preparation of large-area uniform silicon nanowires arrays through metal-assisted chemical etching. *Journal of Physical Chemistry C*. 2008;**112**:4444-4450

- [38] Zhong X, Qu Y, Lin YC, Liao L, Duan X. Unveiling the formation pathway of single crystalline porous silicon nanowires. *ACS Applied Materials & Interfaces*. 2011;**3**:261-270
- [39] To WK, Tsang CH, Li HH, Huang Z. Fabrication of n-type mesoporous silicon nanowires by one-step etching. *Nano Letters*. 2011;**11**:5252-5258
- [40] Kooij ES, Butter K, Kelly J. Silicon etching in HNO₃/HF solution: Charge balance for the oxidation reaction. *Journal of Electrochemical and Solid-State Letters*. 1999;**2**:178-180
- [41] Turner DR. On the mechanism of chemically etching germanium and silicon. *Journal of the Electrochemical Society*. 1960;**107**:810-816
- [42] Cullis AG, Canham LT, Calcott PD. The structural and luminescence properties of porous silicon. *Journal of Applied Physics*. 1997;**82**:909
- [43] Lin L, Guo S, Sun X, Feng J, Wang Y. Synthesis and photoluminescence properties of porous silicon nanowire arrays. *Nanoscale Research Letters*. 2010;**5**:1822-1828
- [44] Kontkiewicz AJ, Kontkiewicz AM, Siejka J, Sen S, Nowak G, Hoff AM, Sakthivel P, Ahmed K, Mukherjee P, Witanachchi S, Lagowski J. Evidence that blue luminescence of oxidized porous silicon originates from SiO₂. *Applied Physics Letters*. 1994;**65**:1436
- [45] Zhao Y, Yang D, Sang W, Li D, Jiang M. Photoluminescence of oxidized porous silicon under UV-light illumination. *Materials Science and Engineering B*. 2005;**116**:95-98
- [46] Bai ZG, Yu DP, Wang JJ, Zou YH, Qian W, Fu JS, Feng SQ, Xu J, You LP. *Materials Science and Engineering B*. 2000;**72**:117
- [47] Lin LH, Sun XZ, Tao R, Li ZC, Feng JY, Zhang ZJ. Femtosecond inverse Faraday effect in magnetic ionic liquid [bmim]FeC₁₄. *Journal of Applied Physics*. 2011;**110**:073109
- [48] Bashouti MY, Pietsch M, Brönstrup G, Sivakov V, Ristein J, Christiansen S. Heterojunction based hybrid silicon nanowire solar cell: Surface termination, photoelectron and photoemission spectroscopy study. *Progress in Photovoltaics*. 2014;**22**:1050-1061
- [49] Dai X, Chen T, Cai H, Wen H, Sun Y. Improving performance of organic-silicon heterojunction solar cells based on textured surface via acid processing. *ACS Applied Materials & Interfaces*. 2016;**8**:14572-14577
- [50] He J, Gao PQ, Liao MD, Yang X, Ying ZQ, Zhou SQ, Ye JC, Cui Y. Realization of 13.6% efficiency on 20 μm thick Si/organic hybrid heterojunction solar cells via advanced nano-texturing and surface recombination suppression. *ACS Nano*. 2015;**9**:6522-6531
- [51] Kim E, Cho Y, Sohn A, Hwang H, Lee YU, Kim K, Park HH, Kim J, Wu JW, Kim DW. Mie resonance-modulated spatial distributions of photogenerated carriers in poly(3-hexylthiophene-2,5-diyl)/silicon nanopillars. *Scientific Reports*. 2016;**6**:29472
- [52] Choi D, Choi A, Seo JH, Seo K. Embedded metal electrode for organic-inorganic hybrid nanowire solar cells, Han-Don Um. *ACS Nano*. 2017;**11**:6218-6224

- [53] Liu R, Wang J, Sun T, Wang M, Wu C, Zou H, Song T, Zhang X, Lee ST, Wang ZL, Sun B. Silicon nanowire/polymer hybrid solar cell-supercapacitor: A self charging power unit with a total efficiency of 10.5%. *Nano Letters*. 2017;**17**:4240-4247
- [54] Zhang J, Zhang Y, Song T, Shen X, Yu X, Lee ST, Sun B, Jia B. High-performance ultrathin organic-inorganic hybrid silicon solar cells via solution-processed interface modification. *ACS Applied Materials & Interfaces*. 2017;**9**:21723-21729
- [55] Sharma M, Pudasaini PR, RuizZepeda F, Elam D, Ayon AA. Ultrathin, flexible organic-inorganic hybrid solar cells based on silicon nanowires and PEDOT:PSS. *ACS Applied Materials & Interfaces*. 2014;**6**:4356-4363

IntechOpen